Supporting Information

Emergent Unusual Ferromagnetism and Insulator-Metal Transition in δ-Doped Ultrathin Ruthenates

Zeeshan Ali[1], Mohammad Saghayezhian[1], Zhen Wang[1,2], Andrew O'Hara[3], Donghan Shin[3], Wenbo Ge[4], Ying Ting Chan [4], Yimei Zhu[2,*], Weida Wu[4], Sokrates T. Pantelides[3,5,*], Jiandi Zhang[1,6,*]

[1]*Department of Physics & Astronomy, Louisiana State University, Baton Rouge, Louisiana 70803, USA.*
[2]*Condensed Matter Physics & Materials Science, Department, Brookhaven National Laboratory, Upton, New York 11973, USA.*
[3]*Department of Physics and Astronomy, Vanderbilt University, Nashville, Tennessee 37235, USA.*
[4]*Department of Physics and Astronomy, Rutgers University, Piscataway, New Jersey 08854, USA.*
[5]*Department of Electrical Computer Engineering, Vanderbilt University, Nashville, Tennessee 37235, USA.*
[6]*Beijing National Laboratory for Condensed Matter Physics, Institute of Physics, Chinese Academy of Sciences, 100190 Beijing, China.*

*Corresponding authors: jiandiz@iphy.ac.cn; pantelides@vanderbilt.edu; zhu@bnl.gov

Supplementary Note 1: CRO film X-ray diffraction

X-ray diffraction was performed on a PanAlytical X'Pert thin-film diffractometer with Cu Kα−1 radiation with a single-crystal monochromator. **Figure S1(a)** shows a coupled (θ-2θ) scan around STO) $(001)_{pc}$ Braggs reflection for 40 u.c. CRO film. We can perceive substrate and film peaks along with Laue interference fringes, confirming the good crystallinity of thin films. The measured out-of-plane (OP) pseudocubic lattice parameter of CRO film from Bragg's peak is ~3.83 Å. This is consistent with the fact that the OP parameter decreases (bulk pseudo-cubic CRO OP ~3.85 Å) to accommodate the lattice mismatch due to tensile strain. Moreover, the FWHM of film and substrate indicates high crystallinity [see **Figure S1(b-c)**]. The film is fully strained to the substrate as $Q_{||}$ of film and substrate is identical as shown in **Figure S1(d)**. Moreover, the core-level spectra are indicative of high-quality film epitaxy, and optimal film stoichiometry [see **Figure S1(e-g)**].

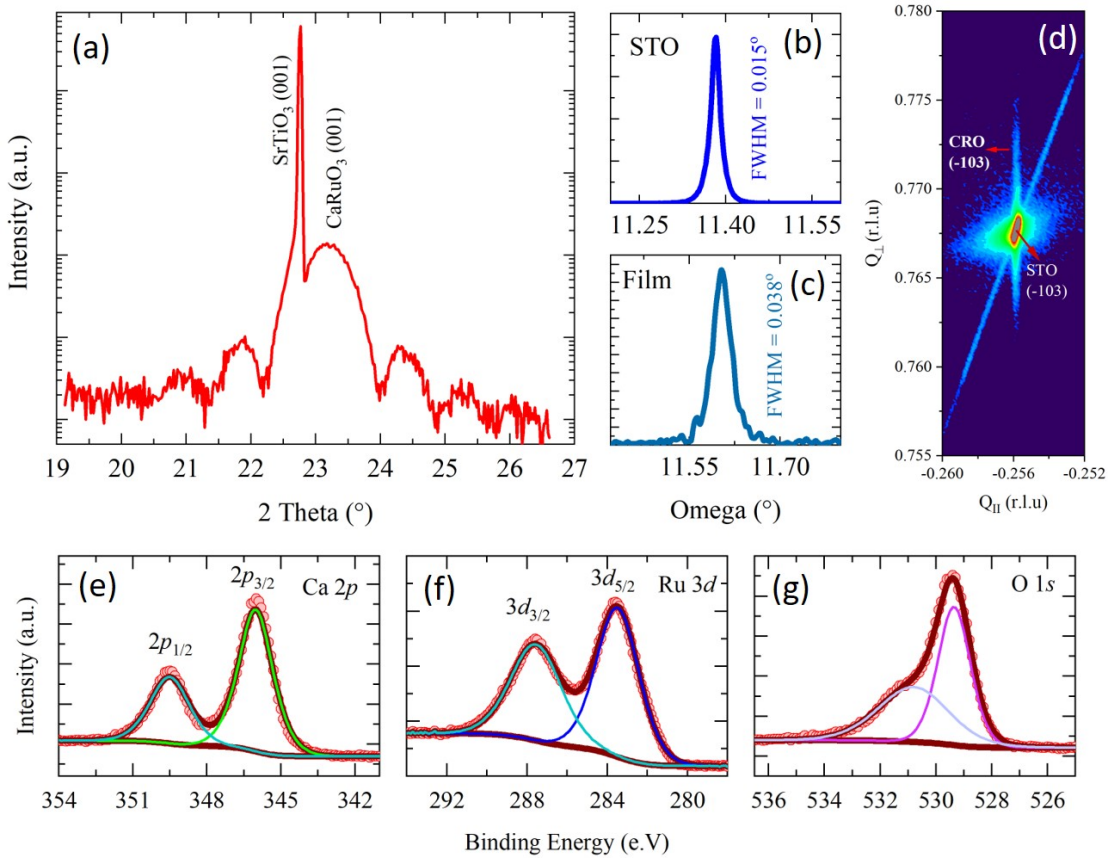

Figure S1. (a) Coupled symmetric (θ-2θ) XRD scan of 40 u.c. CRO film. The presence of thickness fringes confirms high-quality hetero-interface and film surface. (b)-(c) Rocking curve around substrate/film $[001]_c$ and film, respectively. (d) Reciprocal space mapping (RSM) around (-103) of STO substrate. X-ray photoelectron spectroscopy (XPS) for the (e) Ca 2*p*, (f) Ru 3*d* core levels, and (g) O 1*s* spectra for 40 u.c. CRO film.

Supplementary Note 2: Scanning transmission electron microscopy (STEM) and electron energy loss spectroscopy (EELS)

We performed STEM imaging and EELS mapping in several different regions of the δ-doped CRO^{7}-SrO-CRO^{8} heterostructure, as these shown in **Figure S2** and **Figure S3**. The results further confirm that the heterostructure has homogeneous SrO layer and coherent interfaces. The EELS data further confirm that the SrO monolayer is uniform too. The intermixture between Ca and Sr is very minimal. One interesting observation is that Sr is more likely to diffuse to the top CRO rather than the bottom layer (see the EELS maps in **Figure S3**).

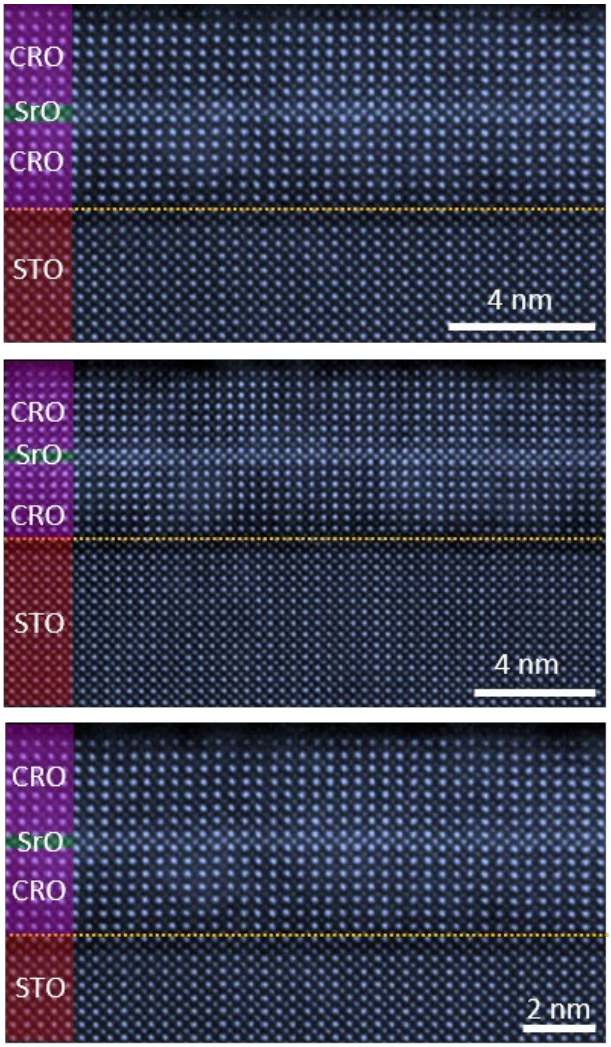

Figure S2. Atomic-scale structure of the δ-doped CRO^{7}-SrO-CRO^{8} heterostructure by STEM across three different regions. The large area STEM-imaging confirms a uniform, and coherent heterostructure. Moreover, due to the atomic intensity proportionality to atomic number Z^2 in HAADF imaging, the Sr (Z=38) atoms are brighter than Ca (Z=20), confirming presence of homogenous Sr monolayer.

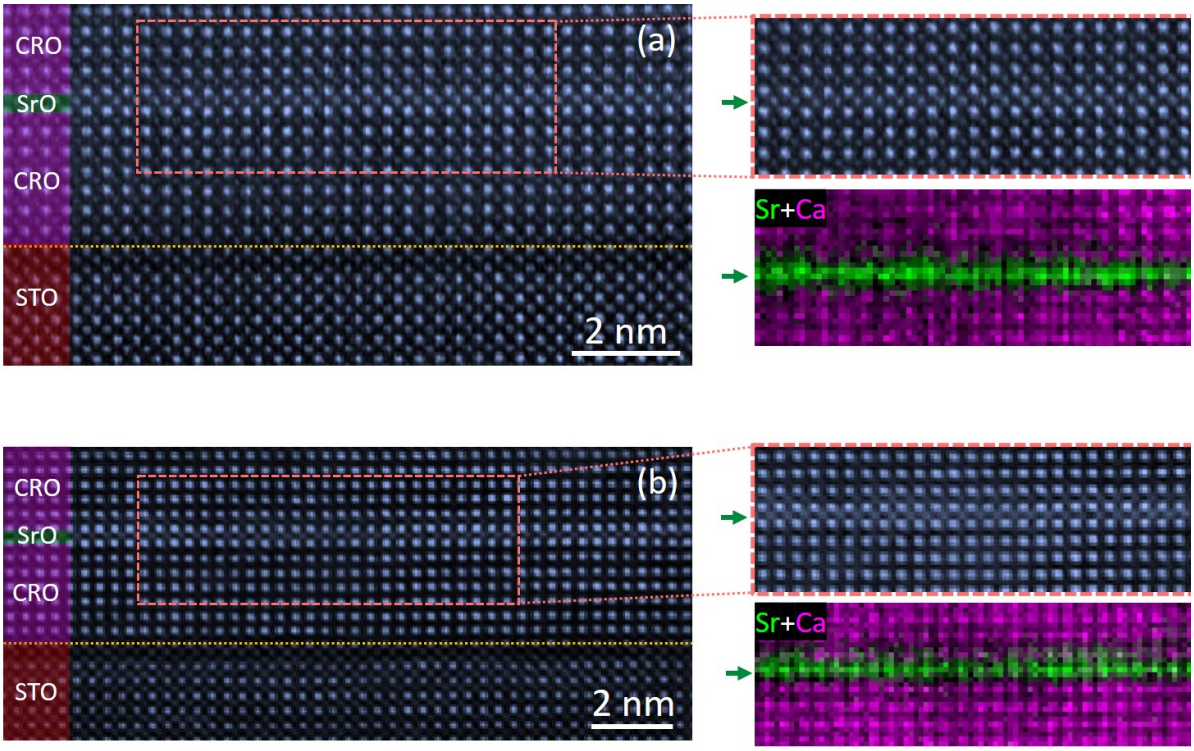

Figure S3. EELS elemental maps of CRO[7]-SrO-CRO[8] heterostructure: (a)-(b) Annular dark-field STEM image and corresponding EELS map for Ca (purple), and Sr (green) from the marked rectangular area. In the large area STEM-imaging, the brighter Sr -atomic monolayer could be observed. Furthermore, the unintegrated EELS map of the region with purple for Ca, and green for Sr establishes Sr is confined to single layer.

Supplementary Note 3: Determination of structural distortions

In most perovskites (ABO_3), the A and B cations radii mismatch often leads to a strain buildup along A-O and B-O bonds, though the strain is accommodated via BO_6 octahedral rotations. These rotations are often explained by Glazer notation ($a^xb^xc^x$)[1], which describes rotations of the octahedra about three orthogonal pseudo-cubic crystallographic axes: $[100]_{pc}$, $[010]_{pc}$, and $[001]_{pc}$. The relative BO_6 rotational magnitude about an axis is represented by letters *a*, *b*, and *c*. The superscript *x* refers to whether adjacent octahedral around one given axis can rotate in-phase (+), out-of-phase (–), or no rotation (0). In Glazer notation, the orthorhombic CRO and SRO exhibit $a^+b^-b^-$ [*Pbnm* (No. 62)][2] patterns as shown in **Figure S4**. This implies that octahedral rotations are in-phase around $[100]_{pc}$ || $[001]_O$, and out-of-phase about the $[010]_{pc}$ || $[1\text{-}10]_O$ and $[001]_{pc}$ || $[110]_O$.

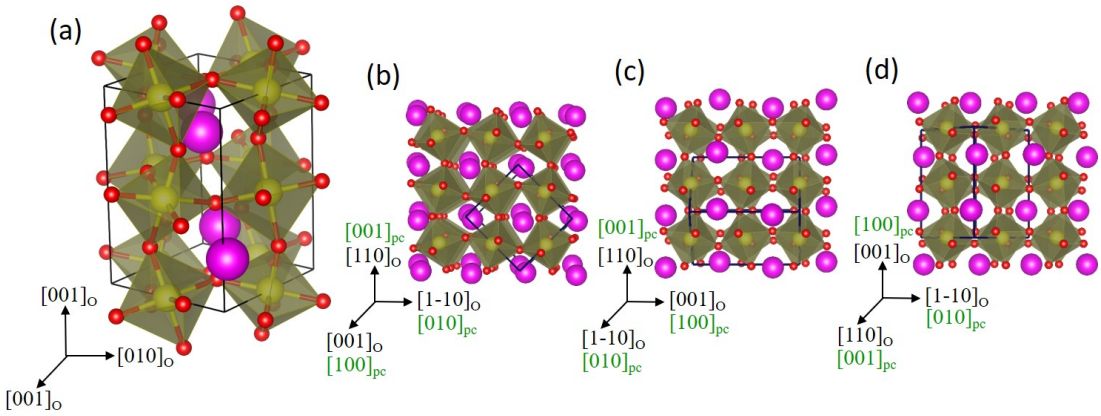

Figure S4. Orthorhombic bulk structure of (a) $CaRuO_3$. (c)-(d) Schematics of $a^+b^-b^-$ rotational pattern. The octahedral rotations are (b) in-phase around $[001]_O$ ($[100]_{pc}$), (c) out-of-phase about $[1\text{-}10]_O$ ($[010]_{pc}$), and (d) $[110]_O$ ($[001]_{pc}$). Orthorhombic (O) and pseudo-cubic (pc) unit cells are denoted by the subscripts.

As illustrated in **Figure S5**, the CRO films grows in $[110]_O$ direction on the cubic STO substrate.[2] Either in-phase ($[100]_{pc}$) or out-of-phase ($[010]_{pc}$) axis can align with the $[100]_S$ direction of the STO substrate, generating domain structure in the film. Here the subscripts designate the orthorhombic (O), pseudo-cubic (pc) unit cell, and STO substrate (s). In domain A type structure, the in-phase rotation (+) pseudo-cubic $[100]_{pc}$ axis is aligned with the $[100]_S$ [see **Figure S5(a-b)**], thus following substrate-film orientation relation holds:

- CRO $[001]_O$ ($[100]_{pc}$) || $[100]_S$
- CRO $[1\text{-}10]_O$ ($[010]_{pc}$)|| $[010]_S$
- CRO $[110]_O$ ($[001]_{pc}$) || $[001]_S$

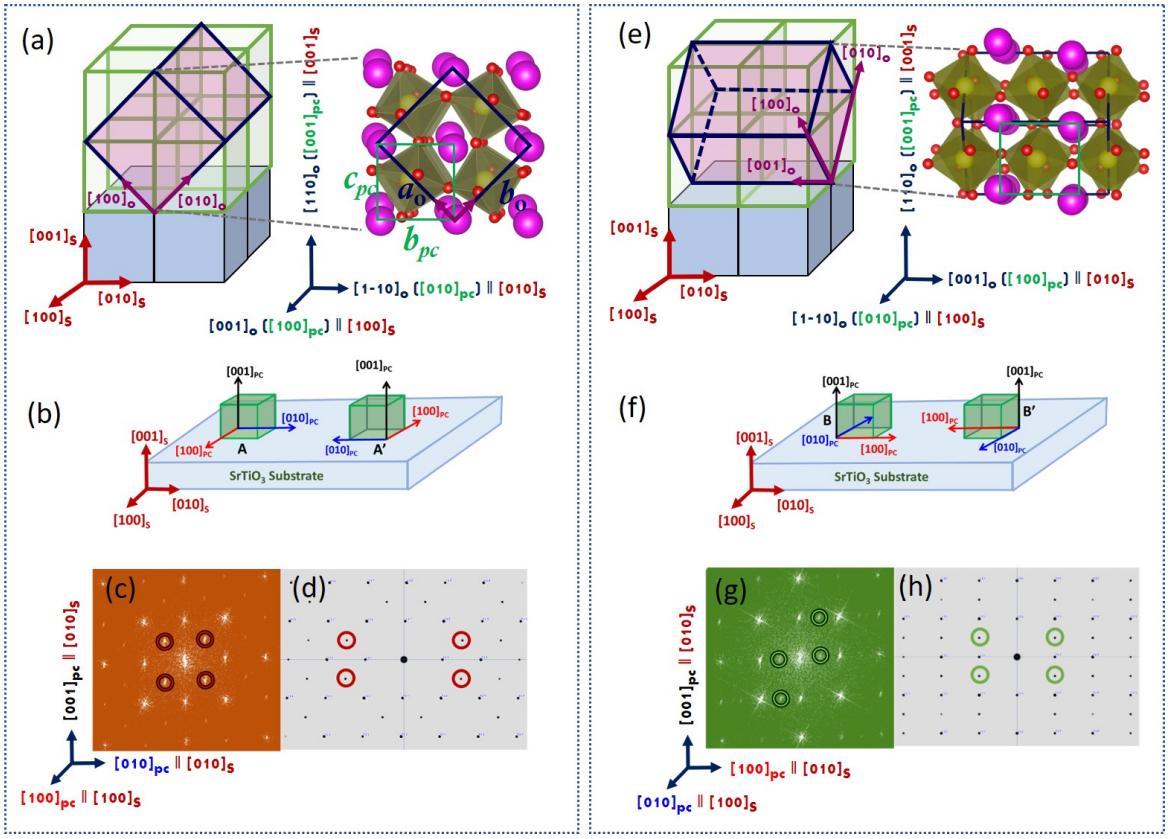

Figure S5. (a) Schematic illustration of $CaRuO_3$ film with $[110]_O$ growth on a cubic $SrTiO_3$ substrate with CRO $[001]_O$ ($[100]_{pc}$) || $[100]_S$ (b) Representation of Domain A, whereas the in-phase rotation (+) film pseudocubic $[100]_{pc}$ axis (marked red) aligns with $[100]_S$. (c) Fast Fourier Transform (FFT) and (d) simulated electron diffraction patterns along in-phase rotation axis: $[100]_{pc}$ || $[100]_S$. (e) Illustration of $CaRuO_3$ film on $SrTiO_3$ substrate with orientation: CRO $[1\text{-}10]_O$ ($[010]_{pc}$) || $[100]_S$. (f) Representation of domain B, whereas in-phase rotation (+) pseudocubic $[100]_{pc}$ axis is parallel with $[010]_S$. (g) FFT and (h) simulated diffraction patterns with electron the beam perpendicular to the in-phase rotation axis, i.e. $[010]_{pc}$ || $[100]_S$.

In domain B, the CRO $[010]_{pc}$ out-of-phase rotation axis is parallel with $[100]_S$ [see **Figure S5(e-f)**], and orientation follows:

- CRO $[1\text{-}10]_O$ ($[010]_{pc}$)|| $[100]_S$
- CRO $[001]_O$ ($[100]_{pc}$) || $[010]_S$
- CRO $[110]_O$ ($[001]_{pc}$) || $[001]_S$

The structure in domains A and B are equal, but with 90° rotation.

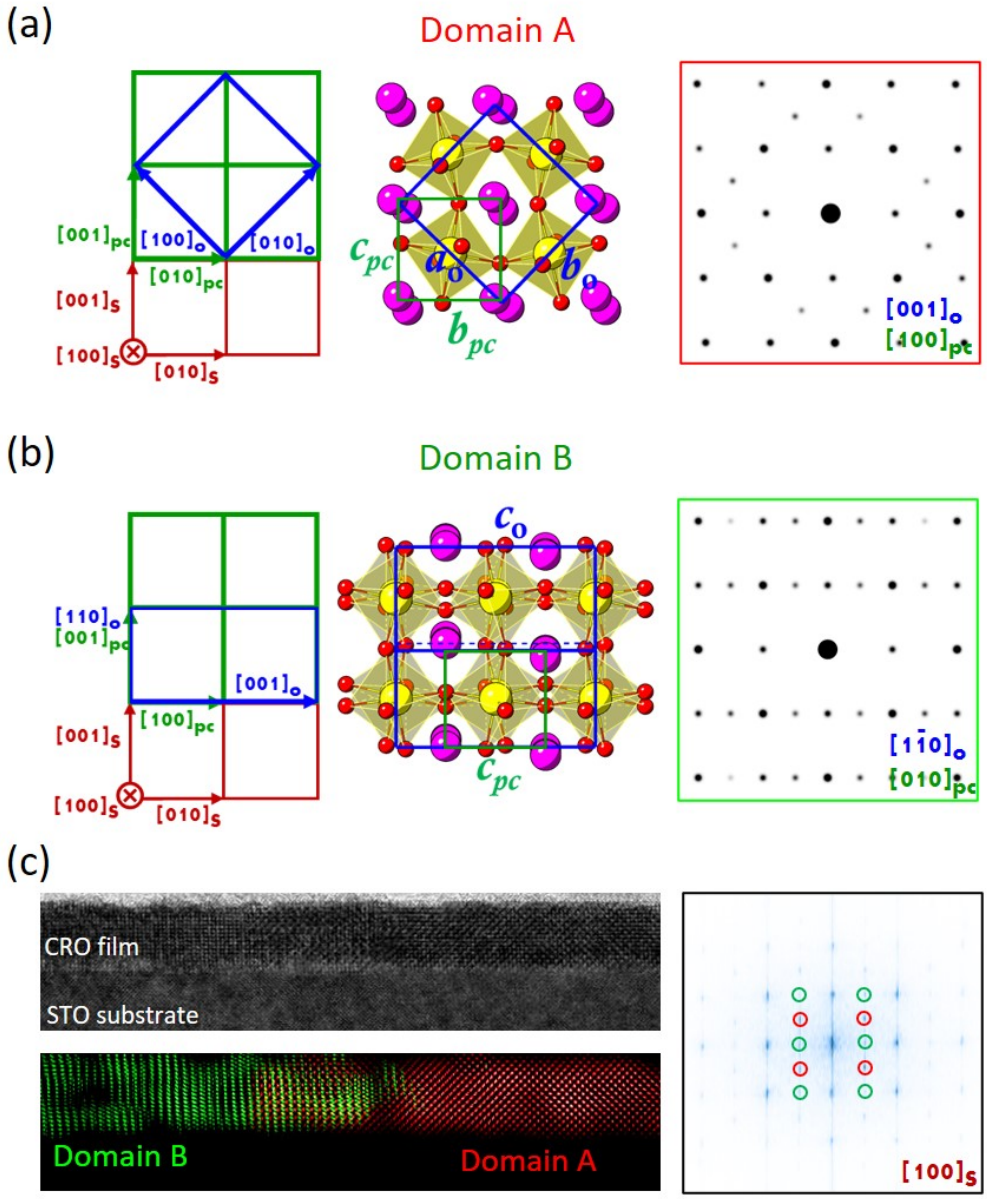

Figure S6. (a-b) Domain A and Domain B projected along the $[100]_S$ direction. Left: illustration of orientation. Middle: projected structure. Right: simulated kinematic electron diffraction pattern of CRO. (c) Top: High-resolution TEM (HRTEM) image of the heterostructure taken along the $[100]_S$ direction. FFT pattern of the HRTEM image inserted. The red and green circles mark the fractional spots corresponding to domain A and domain B. Bottom: Inverse FFT image generating from the fractional spots in (b), displaying the distribution of Domain A and B in the film.

Domain A and B structures are confirmed by the Fast Fourier Transform (FFT) results obtained from high-resolution TEM (HRTEM) image shown in **Figure S6**. The FFT pattern shown in **Figure S5(c)** is consistent with the simulated diffraction pattern of Domain A as in **Figure S5(d)**. This confirms the presence of domain A type unit-cell symmetry, where CRO $[100]_{pc}$ in-phase rotation axis is parallel with $[100]_S$. The consistency of the fractional spots (marked in green) in **Figure S5(g-h)** confirms domain B structural variant.

Viewing along the $[001]_S$ direction, we can acquire CRO film structural information in $[100]_{pc}$ direction from domain A and $[010]_{pc}$ direction from domain B simultaneously, as shown in **Figure S6**. The structure of domain A and B is identical, but when viewing simultaneously along the $[001]_S$ direction the RuO_6 tilt can be observed in domain A because the in-phase (+) octahedral rotation axis is parallel to [100]-STO [see **Figure S6(a)** and **Figure 2(a)**]. On the other hand, for domain B, the electron beam incident along the out-of-phase (-) octahedral rotation axis, and hence the octahedra rotation/tilt could not be resolved in the ABF image because of oxygen overlapping [see **Figure S6(b)**]. However, the A-site cation displacements due to orthorhombic distortion can be measured[3], showing a zigzag pattern [see **Figure 2(b)**].

Supplementary Note 4: STEM imaging of undoped CRO films

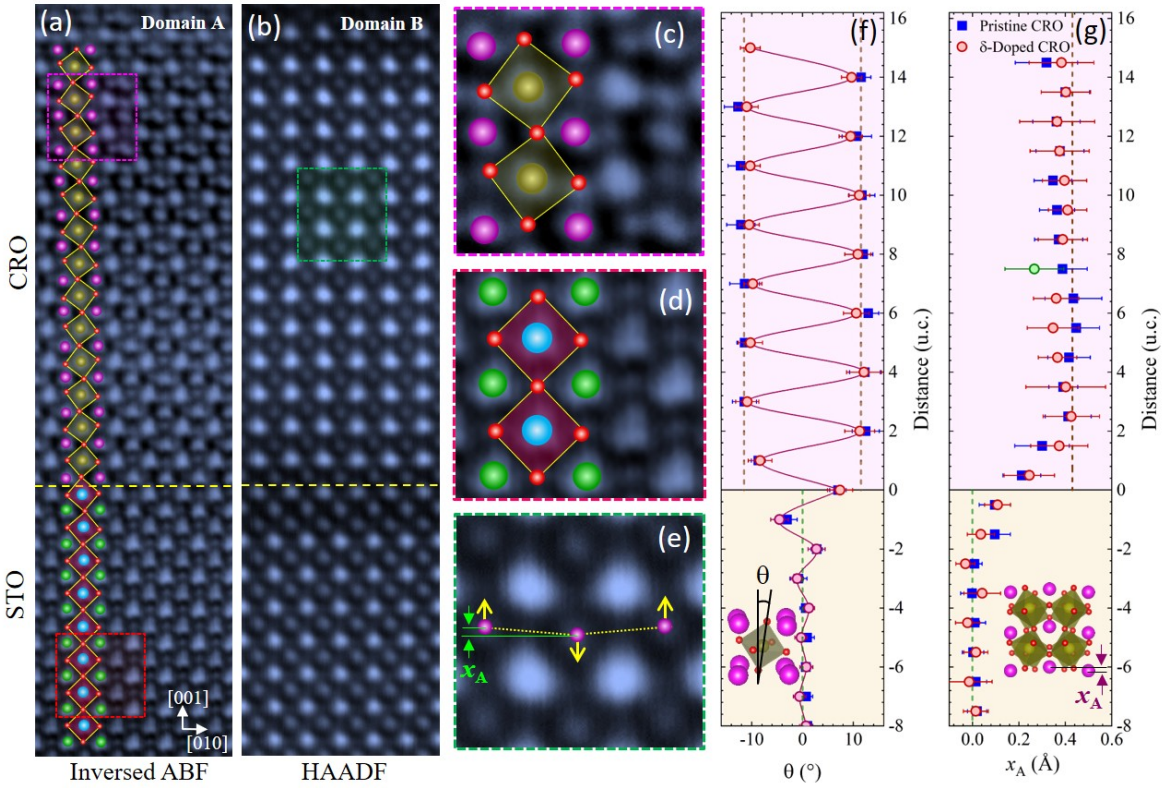

Figure S7. Undoped CRO 15 u.c. (CRO[15]) film STEM images: (a) intensity-inversed ABF, and (b) HAADF images. (c-d) Zoomed in portion of regions marked in panel (a) superimposed with projected octahedra shape. (e) Zoom-in image of the area marked in (b) overlaid by the corresponding A-site cation displacement (x_A), whereas the arrows in (e) mark the A-site displacement direction thus forming an up-down buckling pattern in AO plane. (f-g) Projected octahedral tilt angle (θ) (f), and A-site cation displacement (x_A) (g) as a function of distance from interface of pristine CRO[15] and δ-doped CRO [CRO[7]-SrO-CRO[8]]. The dashed lines in (f) and (g) represent the projected tilt angle, and A-site cation displacements of bulk CRO (brown) and STO (green), respectively.

Atomic-resolved STEM images of undoped CRO 15 u.c. (CRO[15]) film is shown in **Figure S7**. The pristine CRO film shows similar domain structures as those observed in the δ-doped CRO heterostructure [see **Figure S7(a-e)**]. Overall, the HAADF and inversed ABF images corroborate that the film has coherent interface. The statistical analysis establishes that RuO_6 octahedral projected tilt angle (θ) of ~11° [Domain A-type; see **Figure S7(a)**, **Figure S7(c)**, and **Figure S7(f)**] except in the vicinity of film-substrate hetero-interface. On the other hand, the δ-doped CRO heterostructure carries an equivalent RuO_6 octahedral projected tilt angle of ~11°, suggesting that octahedral network structure is not altered by SrO interlayer insertion as in **Figure S7(f)**. Moreover, from domain B structure [see **Figure S7(b)** and **Figure S7(e)**], we have obtained A-site displacements x_A as function of distance from interface as shown in **Figure S7(g)**. The undoped CRO film carries a nearly constant x_A of 0.39 ± 0.05 Å. In contrast, the δ-

doped CRO film preserves an identical trend of x_A (~ 0.38 ± 0.07 Å) for Ca-cation, through the x_A at SrO layer inserted in the CRO is a little smaller ~0.26 ± 0.10 Å. The observation suggests a small local structural modification in the SrO layer.

Supplementary Note 5: Electric transport

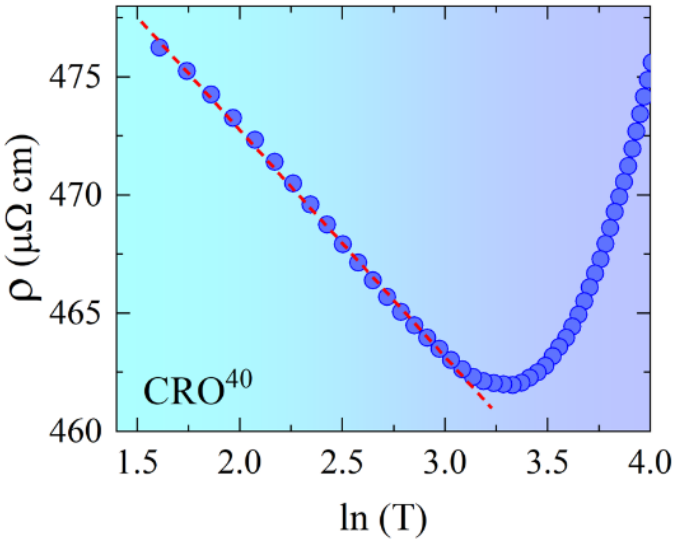

Figure S8. CRO 40 u.c. resistivity versus logarithm of temperature. The red solid line is the linear fit.

The 40 u.c. CRO film shows metallicity with a low temperature resistivity minimum. The resistivity upturn could arise from phenomenon such as weak localization (WL), or electron-electron correlations (EECs).[4,5] In disordered systems, weak-localization is caused by the quantum-interference of conducting electrons on systems defects leads to enhanced backscattering of the conducting electrons, and producing a resistivity upturn. Therefore, WL in 2D system outcomes in a quantum correction to conductivity, which possesses characteristic logarithmic: ln (T) dependence.[4] The effect of weak localization is an outcome of electron interference with itself, however, the wavefunctions of different electrons can also interfere. Consequently, in disordered systems, increased carrier scattering diminishes the effective electron screening, thereby leading to EEC enhancement and a broad opening of the Coulombic gap possessing a zero density of states.[5,6] We refer to it as quantum mechanical EEC correction to conductivity, whereas in 2D systems, the conductivity scales with temperature logarithm.[4] **Figure S8** shows that the low-temperature resistivity upturn of CRO^{40} indeed scales well with ln T. Considering that a uniform magnetic field destroys electrons waves coherence via de-phasing, thus suppressing the localization effect in WL, which causes a negative magnetoresistance as oppose to EEI insensitivity to magnetic fields holding a positive magnetoresistance.[4,7,8] Therefore, the presence of negative MR in CRO^{40} [see **Figure 3(d)**] supports that the resistivity upturn in CRO^{40} is caused by weak localization.

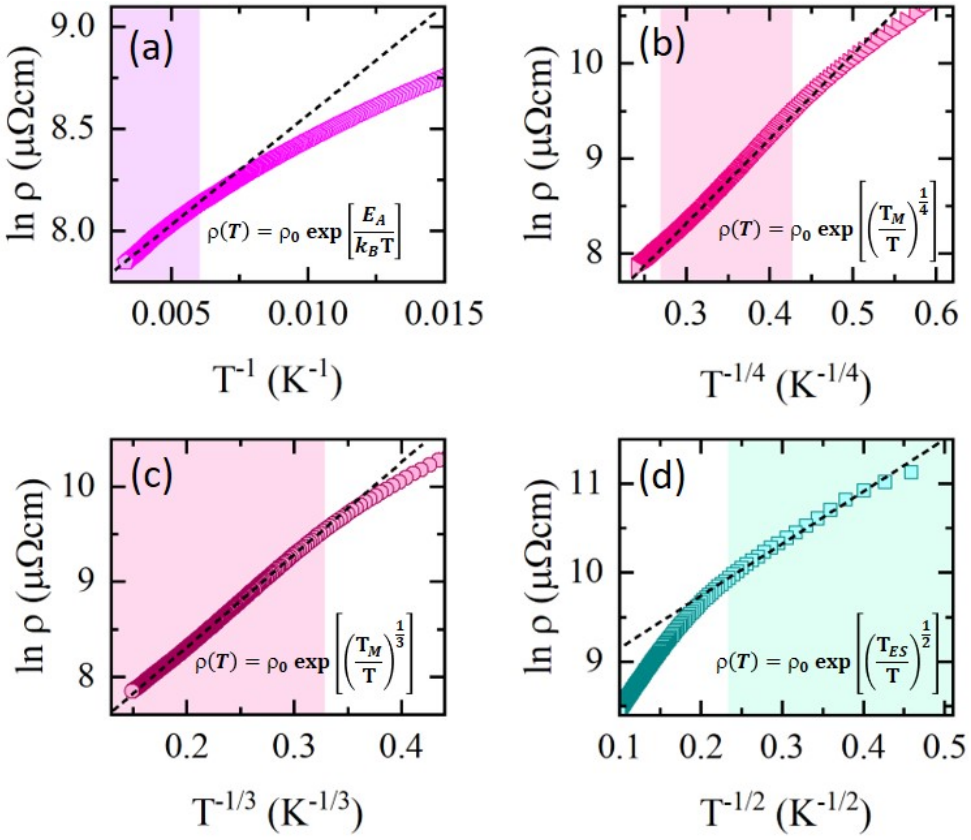

Figure S9. CRO 15 u.c. logarithmic resistivity versus (a) T^{-1} (thermal activation model), (c) $T^{-1/4}$ (3D-Mott VRH), (c) $T^{-1/3}$ (2D-Mott VRH), and (a) $T^{-1/2}$ (Efros VRH). The dashed line is the linear fit.

In the Anderson-type insulating state, the electron hopping to the nearest neighbor sites is restricted, since electronic thermal energy is smaller as compared to the energy difference between adjacent localized states, which means that electrons cannot overcome the energy barrier caused by disorder, and thus hopping to the far localized site is not probable. Though, to hop, the electrons have to locate a site, where the difference of energies between the two localized sites is small, which leads to variable range hopping (VRH) conduction. Mott categorized this phenomenon with resistivity scaling as: $\rho\,(T) = \rho_0 \exp\left[\left(\frac{T_M}{T}\right)^{\frac{1}{d+1}}\right]$. Here, d is system dimensionality: d = 1, 2, 3, and $T_M = \frac{\beta_M}{N(E_F)\xi^d k_B}$ is Mott characteristic temperature [β_M, ξ and $N(E_F)$ is constant, localization length, and Fermi-level density of states, respectively].[9,10] In Mott-type VRH, the Coulomb interaction between hopping sites is ignored, thus the density of states near Fermi level is considered as a constant. However, in Efros and Shklovskii variable range hopping (ES-VRH), where Coulombic interactions are taken into consideration, the *e-e* interactions lead to a Coulomb gap at low temperatures. In this case, the

resistivity in all dimensions scales as: $\rho\,(T) = \rho_0 \exp\left[\left(\frac{T_{ES}}{T}\right)^{\frac{1}{2}}\right]$, here; $T_{ES} = \beta_{ES}\, e^2/\varepsilon\, k_B\, \xi$ is a Efros characteristic temperature with β_{ES}= 2.8, ξ is localization length, e elementary charge, and ε dielectric constant.[5,9,10]

To detect the temperature exponent for transport of CRO[15], we considered four conduction models. The thermal activation: $\rho\,(T) = \rho_0\, e^{E_A/k_BT}$, where ρ_0 is the resistivity coefficient, and E_A is the activation energy [see **Figure S9(a)**]. The 2D-Mott VRH $\rho\,(T) = \rho_0\, e^{(T_M/T)^{1/3}}$, and 3D-Mott VRH $\rho\,(T) = \rho_0\, e^{(T_M/T)^{1/4}}$, where T_M is Mott temperature [see **Figure S9(b-c)**]. The Efros VRH $\rho\,(T) = \rho_0\, e^{(T_{ES}/T)^{1/2}}$, where T_{ES} is Efros temperature [see **Figure S9(d)**]. In the high temperature range, thermal activation and 3D Mott-VRH could not produce a decent linear curve of logarithmic resistivity versus T^{-1} and $T^{-1/4}$, respectively [see **Figure S9(a-b)**]. However, the CRO[15] resistivity is well described by 2D Mott-VRH [$\ln(\rho) \propto T^{-1/3}$] as shown in **Figure S9(c)**. Decreasing the temperature, near ~25 K [see **Figure S9(c-d)**] a crossover in the scaling of CRO[15] resistivity is observed, from Mott-type 2D variable hopping [$\ln(\rho) \propto T^{-1/3}$] range to Efros-type VRH [$\ln(\rho) \propto T^{-1/2}$]. Theoretically the cross over temperature is given as[11]: $T_{cross} = \frac{16\, T_{ES}^2}{T_M}$, using $T_{ES} \approx 33$ K, and $T_M \approx 820$ K, obtained from experimental data fittings, we get $T_{cross} \approx 22$ K, which is within experimentally detected cross over range. Nevertheless, the presence of Efros-type VRH validates that at sufficiently low temperatures, EECs probably play a significant role.

Supplementary Note 6: Magnetic force microscopy

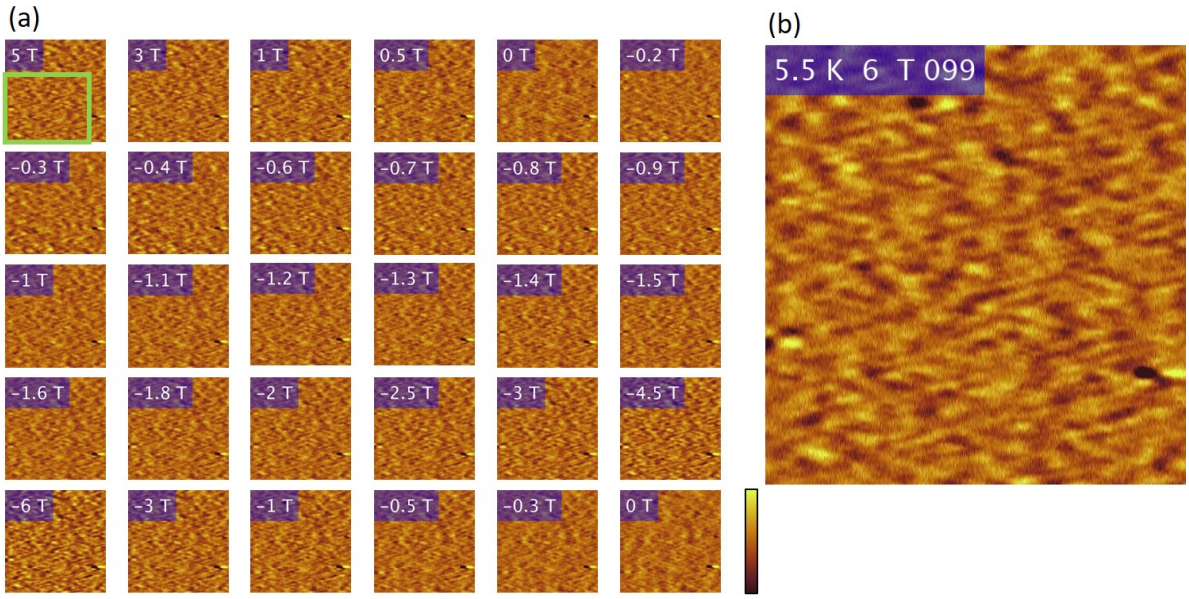

Figure S10. Unprocessed field-dependent MFM images of the δ-doped CRO[10]-SrO-CRO[10] heterostructure taken at 5.5 K with the topography of the scanning area. (a) Sequential MFM images under various external fields at 5.5 K. The green box indicates the scanning area of the MFM images in the main text. The color scale for the MFM data is 0.04 Hz. (b) A snapshot of the scanning area from a topographic imaging video as varying applied magnetic field at T = 5.5 K. The color scale for the topography image is 50 nm.

Dark (bright) regions in MFM images represent attractive (repulsive) magnetization, where magnetization is parallel (antiparallel) with the tip polarization. **Figure S10(a)** shows the unprocessed MFM images. The field is ramped from 5 T to -6 T then back to 0 T. The processed MFM images in the main text are generated in two steps. First, they are cropped from the unprocessed images. The cropped region is labeled by the green box in **Figure S10(a)**. Then, a topographical background has been subtracted from each MFM image to highlight the magnetic contrast uncorrelated with the topography. The MFM data measured at -6 T is used as the topographical background since the sample is magnetically saturated at that field. The topographic image of scanning from the topographic imaging video as varying applied external field is shown in **Figure S10(b)**.

Supplementary Note 7: Anomalous Hall in CRO[10]-SrO-CRO[10] heterostructure

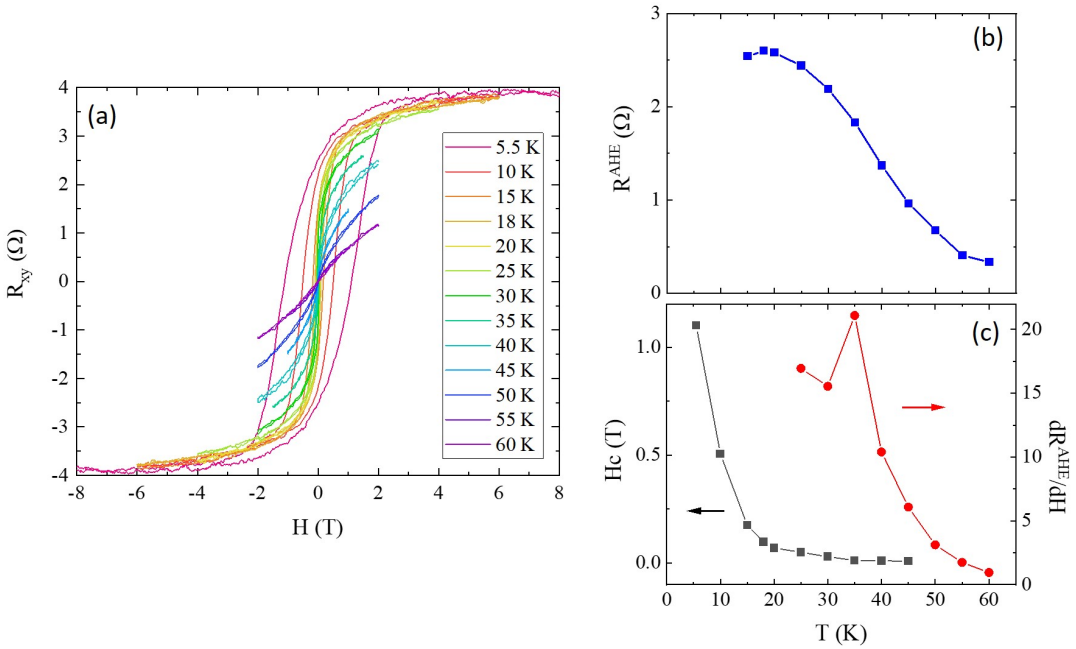

Figure S11. (a) Field dependence of Hall resistance R_{xy} of CRO[10]-SrO-CRO[10] heterostructure at various temperatures from 5.5 to 60 K. The data is anti-symmetrized to remove the contributions from longitudinal components due to the misalignment of contacts. The anomalous Hall effect (AHE) hysteresis loops are getting larger as the temperature decreases. The small loops shown above 35 K are caused by the finite ramp rate of the applied field. (b) Temperature dependence of R_{AHE} (blue triangle). The data are taken from the R^{AHE} (H) curves at H = 0.5 T. (c) Temperature dependence of coercive field Hc (black square) and the initial slope of R^{AHE} (H) curves (red circle). The logarithmic scale shows a significant change of Hc as temperature increases. Above 35 K, the tiny coercive fields are caused by the finite field ramp rate. The initial slopes dR^{AHE}/dH, which are proportional to magnetic susceptibility, are taken from the slopes of $R_{AHE}(H)$ at H = 0. The green dash line exhibits the ordering temperature at 35 K.

The total Hall resistance is given as $R_{xy} = R_0H + R_AM$. Here, the first term represents the ordinary Hall effect, where R_0 is ordinary Hall coefficient due to Lorentz force, and H is the external magnetic field. The second term signifies the anomalous effect ($R^{AHE} = R_AM$), where R_A denotes the anomalous Hall coefficient, and M is the magnetization component. The Hall resistance due to the ordinary effect is proportional to the external magnetic field. The R_{xy} of CRO[10]-SrO-CRO[10] heterostructure at various temperatures is shown in **Figure S11**. The presence of the hysteretic behavior is attributed to the anomalous Hall, thereby providing compelling evidence of ferromagnetic ordering.

Supplementary Note 8: SQUID magnetometry

The magnetization was studied by using Quantum design SQUID (superconducting quantum interference device) reciprocating sample option (RSO). For magnetization as a function of temperature M(T) measurements, the samples were first cooled down to 5 K under the 5000 Oe field, and then the data was acquired while warming in presence of 100 Oe field. The data points were first smoothed using Locally Weighted Scatterplot Smoothing. The M(T) curve of 15, 20, and 40-unit cell of CRO film establishes a paramagnetic-like signal reminiscent of STO substrate with no clear signs of ferromagnetic transition as in **Figure S12**. In contrast, inserting a single SrO layer (δ-doping) in the middle of CRO films induces FM ordering as M(T) represents a paramagnetic to ferromagnetic transition. However, the M(T) curves in the δ-dopped CRO films has rather unusual T-dependence, showing non-typical long-range order M(T) line shape. Weak but finite magnetization values appear below ~ 60 K for these three doped films but their T_c is located at lower temperatures. The samples experience a unusual phase on cooling before entering a FM ordering, consistent with the suggestion of Griffiths-phase described in the main text.

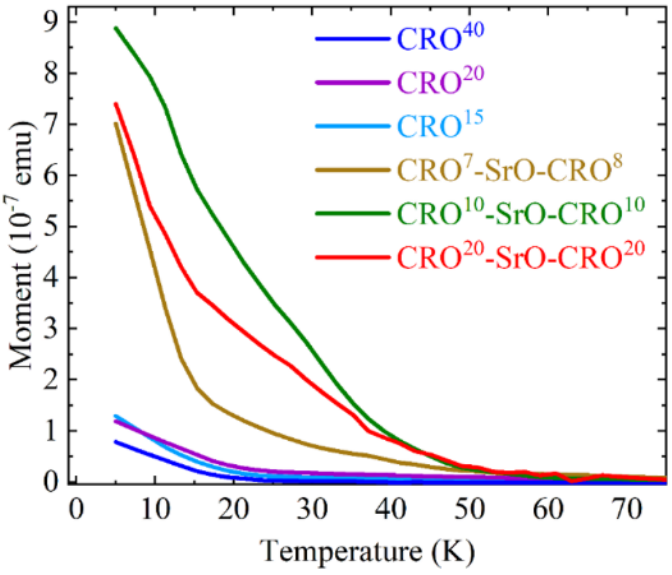

Figure S12. Temperature-dependent magnetization of different thickness of undoped and δ-doped CRO films.

Supplementary Note 9: Density Functional theory

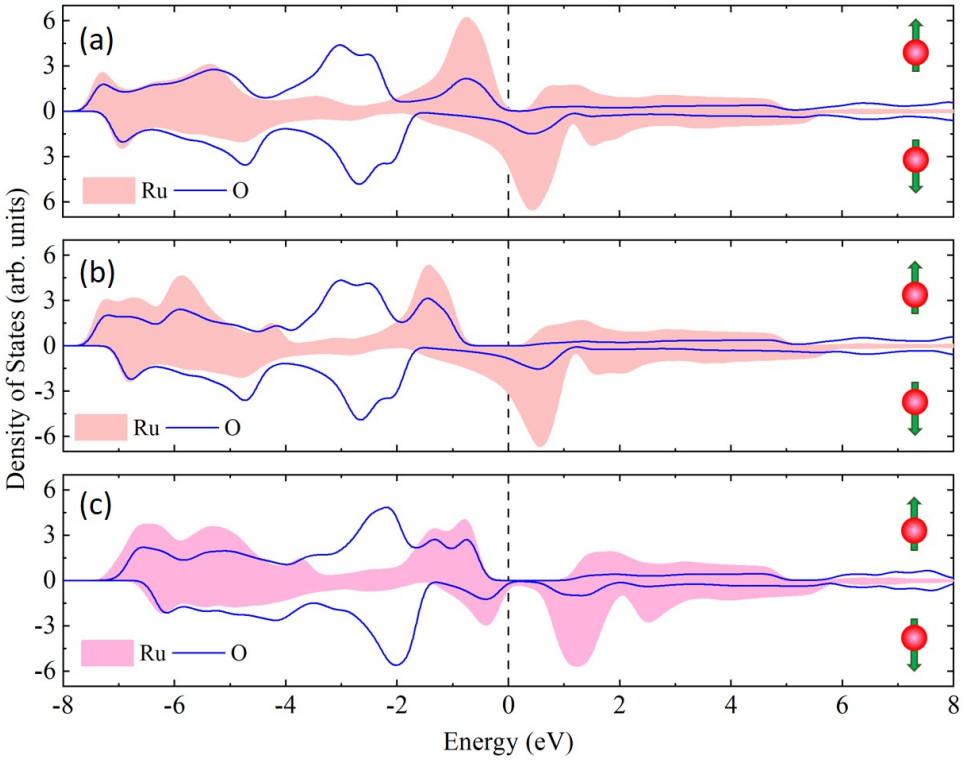

Figure S13. Density states (DOS) of Ru, and O in bulk (a) $SrRuO_3$ with U = 0.6 eV, (b) $SrRuO_3$ with U = 3.5 eV, and (c) $CaRuO_3$ with U = 3.5 eV.

For bulk $SrRuO_3$ (SRO), due to the extended 4*d* orbitals, the correlation effects are expected to be weaker. However, a general agreement is that some additional correlation is necessary for the electronic band structure determination. As per Rondinelli *et al.*[12], the inclusion of electron-electron correlations in the form of the Hubbard term with U = 0.6 eV best describes the bulk (*Pnma*) SRO electronic structure. For SRO, our calculations shown in **Figure S13(a)** reproduce the electronic structure in agreement with the previously published literature.[12] With a U = 0.6 eV, the Ru 4*d* state contribution is completely triggered by the minority spin channel, and the system is almost half-metallic as in **Figure S13(a)**. If the Hubbard U is increased to 3.5 eV [see **Figure S13(b)**] as is commonly done for thin-film heterostructures (discussed below), the majority-spin t_{2g} becomes insulating, while one-third filled minority t_{2g} is conducting, consequently, SRO becomes a half-metal, agreeing with the previous results.[12] However, experimentally, such a half-metallic state in SRO has yet to be observed. With the same value of U = 3.5 eV, CRO's DOS has a larger gap in the O 2*p* and Ru 4*d* states (majority channel) but with a reduced bandwidth; a consequence of the highly tilted octahedral Ru-O-Ru bond angle [see **Figure S13(c)**]. Additionally, in contrast to SRO, this highly distorted octahedral

angle of CRO leads to a smaller value of the DOS at the Fermi-energy DOS [see minority channel DOS in **Figure S13(c)**]. Therefore, as per the Stoner criterion $U\,D(\varepsilon_F) > 1$, this suggests that ferromagnetism is unfavorable.

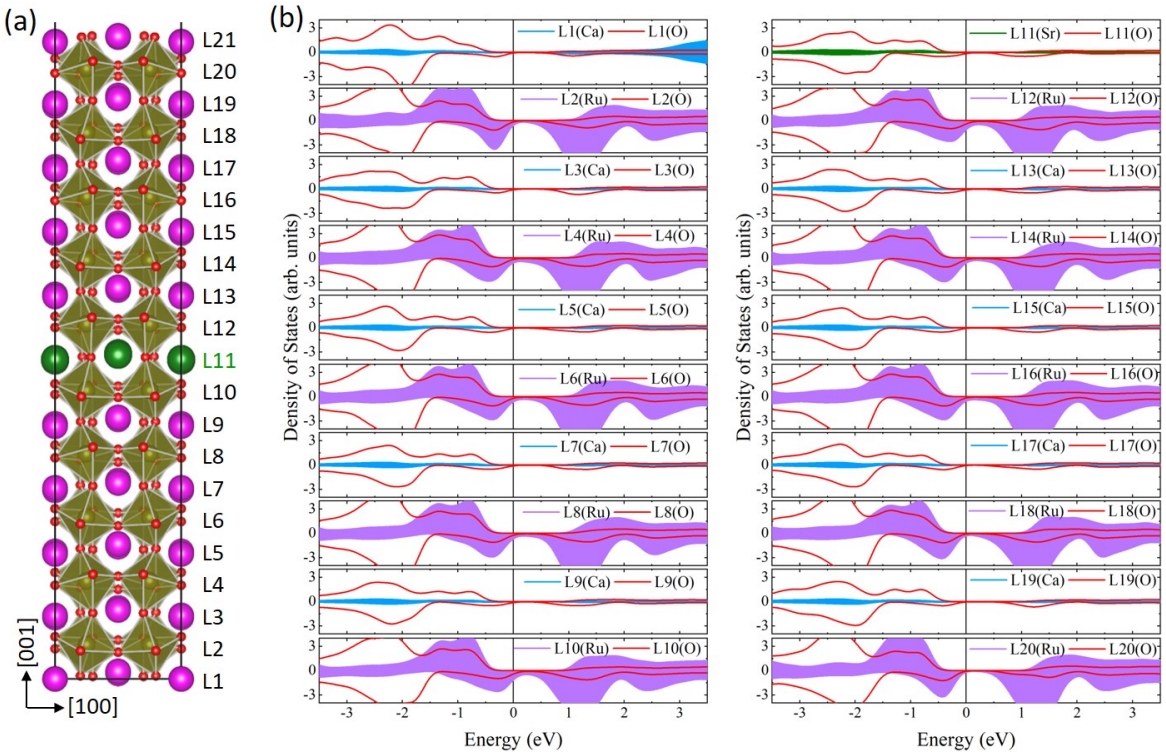

Figure S14. (a) Schematic representation of δ-doped heterostructures, where one of the Ca atomic (blue) layers is replaced by Sr atoms (green). O atoms (red) form an octahedral network, whereas Ru atoms are located at the center of the octahedra. (b) Layer by layer density states (DOS) of the heterostructure, whereas each panel signifies DOS of the individual layer as labeled in panel (a). The up-spins (majority) are represented as positive, and down spins (minority) as negative.

After understanding the bulk SRO and CRO electronic structure, we examine the electronic and magnetic structure of an example heterostructure. For bulk SRO or thicker films, the DFT calculations with Hubbard term U = 0.6 eV can describe the electronic structure, though for ultra-thin SRO films, as previously reported, the theoretical calculations even with U > 3 eV are unable to replicate the previously reported insulating-nonmagnetic state.[13,14] On other hand, Marcos *et al.*[15] calculations with U = 4 eV establish that 1 ML SRO is a minority-spin half-metallic ferromagnet only if surrounded by $SrTiO_3$ lattice. Therefore, to unravel the electronic and magnetic nature of our δ-doped heterostructure [see **Figure S14(a)**], we adopt Hubbard U of 3.5 eV. Such a value of the Hubbard U was also recently used to study few-layer SRO films sandwiched between $BaTiO_3$ in thin-film heterostructures.[16] **Figure S14(b)** displays the results

of the layer-by-layer DOS of δ-doped CRO structure. We found a local DOS enhancement at Fermi energy adjacent to the SrO inserting layer.

REFERENCES

1. Woodward, P. M. Octahedral Tilting in Perovskites. I. Geometrical Considerations. *Acta Crystallogr. Sect. B Struct. Sci.* **53**, 32–43 (1997).
2. Vailionis, A. *et al.* Misfit strain accommodation in epitaxial ABO_3 perovskites: Lattice rotations and lattice modulations. *Phys. Rev. B* **83**, 064101 (2011).
3. Moon, E. J. *et al.* Spatial control of functional properties via octahedral modulations in complex oxide superlattices. *Nat. Commun.* **5**, 5710 (2014).
4. Lee, P. A. & Ramakrishnan, T. V. Disordered electronic systems. *Rev. Mod. Phys.* **57**, 287–337 (1985).
5. Altshuler, B. L., Aronov, A. G. & Lee, P. A. Interaction effects in disordered fermi systems in two dimensions. *Phys. Rev. Lett.* **44**, 1288–1291 (1980).
6. Efros, A. L. & Shklovskii, B. I. Coulomb gap and low temperature conductivity of disordered systems. *J. Phys. C Solid State Phys.* **8**, L49 (1975).
7. Bergmann, G. Weak localization in thin films: a time-of-flight experiment with conduction electrons. *Phys. Rep.* **107**, 1–58 (1984).
8. Lee, P. A. & Ramakrishnan, T. V. Magnetoresistance of weakly disordered electrons. *Phys. Rev. B* **26**, 4009 (1982).
9. Shklovskii, B. I. & Efros, A. L. *Electronic Properties of Doped Semiconductors*. vol. 45 (Springer Berlin Heidelberg, 1984).
10. Gantmakher, V. F. & Man, L. I. *Electrons and Disorder in Solids*. *Electrons and Disorder in Solids* (Oxford University Press, 2005). doi:10.1093/acprof:oso/9780198567561.001.0001.
11. Rosenbaum, R. Crossover from Mott to Efros-Shklovskii variable-range-hopping conductivity in InxOy films. *Phys. Rev. B* **44**, 3599–3603 (1991).
12. Rondinelli, J. M., Caffrey, N. M., Sanvito, S. & Spaldin, N. A. Electronic properties of bulk and thin film SrRuO3: Search for the metal-insulator transition. *Phys. Rev. B* **78**, 155107 (2008).
13. Chang, Y. J. *et al.* Fundamental Thickness Limit of Itinerant Ferromagnetic $SrRuO_3$ Thin Films. *Phys. Rev. Lett.* **103**, 057201 (2009).
14. Xia, J., Siemons, W., Koster, G., Beasley, M. R. & Kapitulnik, A. Critical thickness for itinerant ferromagnetism in ultrathin films of $SrRuO_3$. *Phys. Rev. B* **79**, 140407 (2009).
15. Verissimo-Alves, M., García-Fernández, P., Bilc, D. I., Ghosez, P. & Junquera, J. Highly Confined Spin-Polarized Two-Dimensional Electron Gas in $SrTiO_3/SrRuO_3$ Superlattices. *Phys. Rev. Lett.* **108**, 107003 (2012).
16. Meng, M. *et al.* Interface-induced magnetic polar metal phase in complex oxides. *Nat. Commun.* **10**, 5248 (2019).